ULTRASONIC IMAGING **34,** 93- 109 (2012)

Robust Strain-Estimation Algorithm Using Combined Radiofrequency and Envelope Cross-Correlation with Diffusion Filtering

MOHAMMAD ARAFAT HUSSAIN,[1] S. KAISAR ALAM,[2] SOO YEOL LEE[3] AND MD. KAMRUL HASAN[1, 3]

[1]*Department of Electrical and Electronic Engineering*
Bangladesh University of Engineering and Technology
Dhaka-1000, Bangladesh
khasan@eee.buet.ac.bd

[2]*Riverside Research*
156 William Street
New York, NY

[3]*Department of Biomedical Engineering*
Kyung Hee University
South Korea

In ultrasound elastography, the strain in compressed tissue due to external deformation is estimated and is smaller in harder than softer tissue. With increased stress, the nonaxial motions of tissue elements increase and result in noisier strain images. At high strain, the envelope of the rf signal exhibits robustness to signal decorrelation. However, the precision of strain estimates using envelope signals is much worse compared to that using the rf signals. In this paper, we propose a novel approach for robust strain estimation by combining weighted rf cross-correlation and envelope cross-correlation functions. An applied strain-dependent piecewise-linear-weight is used for this purpose. In addition, we introduce nonlinear diffusion filtering to further enhance the resulting strain image. The results of our algorithm are demonstrated for up to 10% applied strain using a finite-element modelling (FEM) simulation phantom. It reveals that the elastographic signal-to-noise ratio (*SNRe*) and the elastographic contrast-to-noise ratio (*CNRe*) of the strain images can be improved more significantly than with other algorithms used in this paper. In addition, comparative results in terms of the mean structural similarity (MSSIM) using *in vivo* breast data show that the strain image quality can be improved noticeably by the proposed method than with the techniques employed in this work.

KEY WORDS: Diffusion filtering; elastography; envelope; linear weight; strain; stress; ultrasonic imaging.

INTRODUCTION

Elasticity imaging is an emerging medical diagnostic tool for displaying mechanical properties of biological tissues. It is well recognized by medical practitioners that tissue mechanical properties such as stiffness change significantly with changes in tissue pathology. For example, cancerous tissues may be orders of magnitude stiffer than the surrounding normal tissues.[1] Stiffness can be estimated by sophisticated techniques such as elastography, which is showing great promise in the detection and/or characterization of breast and prostate tumors,[1-4] liver cirrhosis,[5] and vascular plaques.[6] The strain image is typically computed as the spatial gradient of local tissue displacements.[2-4, 7-9] Other approaches estimate strain directly from the pre- and postcompression rf echo waveforms or spectra.[10-12] There are other categories of strain estimators, such as hybrid estimators, which combine direct and gradient strain estimators[13] and speckle-tracking-based strain estimators.[14]

0161-7346/12 $18.00

The postcompression rf echo signal experiences compression inside the tissue structure due to applied axial stress.[10] Therefore, the postcompression rf signal is generally modeled as a compressed and delayed version of the precompression rf signal.[10] The direct strain estimation technique in the time domain[10] relies on estimating the compression factor by maximizing the correlation coefficient between the pre- and stretched postcompression echo segments. In Ophir et al[11] and Alam et al,[12] on the other hand, a Fourier-domain-based incoherent strain imaging technique is described that uses cross-correlation analysis to estimate the spectral shift between the pre- and postcompression power spectrum.

Various reported gradient-based strain estimators obtain the strain image from the spatial gradient of the displacement field, computed by the cross-correlation analysis between a pair of the windowed pre- and postcompression signal segments. Since the gradient operation amplifies the high frequency noise due to the large jump in the axial displacement value, the SNRe of the strain image is generally poorer than that of the direct strain estimators.[9, 11] To minimize the gradient noise, a smoothing operation is generally performed over the displacement field before the gradient operation.[9, 15, 16] The smoothing may be performed using a median filter, linear regression[17] or smoothing-spline.[9] Wavelet-based denoising schemes also have been reported,[18, 19] which smooth the displacement and strain map. In Varghese et al,[18] wavelet shrinkage denoising is applied to the displacement estimates and in Chen et al,[19] a similar denoising technique is applied to the strain estimates. Furthermore, to reduce signal decorrelation noise, global stretching[20] by an appropriate factor is applied to the postcompression rf signal to increase the correlation between the pre- and postcompression echo segments, although there is a high probability of missing the hard inclusions in the strain image. In addition, window size and window overlap are two other critical parameters upon which the image resolution and SNR performance depend. In Varghese et al,[21] a two- step (coarse and fine) rf cross-correlation-based strain estimation algorithm is presented to overcome the tradeoff between resolution and SNR performance.

To improve the robustness at high strain, some reported strain estimators use only the envelope or rf signal in conjunction with the envelope for strain estimation.[22-25] In Ophir et al,[22] a theoretical framework is discussed for increasing the dynamic range in the elastogram by using a composite (combination of the rf and envelope) strain-filter approach. The methods of Chen et al[23] and Varghese et al[24] use the pre- and postcompression envelope window cross-correlation to calculate the sparse displacement (seed) in the tissue at the preliminary stage and, in subsequent stages, the primary seeds are used to track the displacement in a gradual finer grid by using the envelope[23] or rf[24] cross-correlation. Since the strain estimation variance is high and the SNRe is low for the envelope signal compared to that of the rf signal at low strain,[22] the preliminary estimated seeds or tracking parameters used in Chen et al[23] and Varghese et al[24] may be misleading at low strain. In Shiina et al,[25] a phase-domain processing technique is proposed where displacement is calculated by combining the information from the phase cross-correlation with that of the envelope cross-correlation.

In this paper, we propose a novel approach for robust strain estimation using a combined piecewise-linear-weighted rf normalized cross-correlation (NCC) and envelope NCC followed by denoising by a diffusion filter. The displacement map computed from the rf echo NCC is known to be 'clean' at low strain while very noisy at high strain due to echo decorrelation. On the other hand, the displacement map computed from the envelope NCC is less precise and often noisy at low strain while robust to echo decorrelation noise at high strain. Our novel algorithm combines the advantages of both approaches by defining an applied-strain dependent piecewise linear weight via which the rf and envelope NCC functions are added to find the final peak. In this algorithm, as applied strain (and consequently, echo decorrelation) increases, the relative contribution of the rf NCC decreases. Instead of a single global stretching, we use nonstretched and globally-stretched postcompression rf echo

windows with a precompression counterpart rf window to find the NCC peak to account for the fact that the rf signal experiences less or no compression in the lesion volume. We also estimate and correct for lateral shift by using the Poisson's ratio.[26] Finally, we introduce diffusion filtering in the field of elastography. A geometric nonlinear diffusion filtering[27] is performed on the calculated strain image. To demonstrate the efficacy of our algorithm, we evaluate and compare the performance of our algorithm with other reported algorithms using simulation data by the FEM simulation data, experimental phantom data and *in vivo* breast data.

METHODS

Signal model

The backscattered ultrasound rf signals before and after compression can be written in the simplified 1-D form as[10]

$$r_1(t) = s_1(t) + \upsilon_1(t) = s(t) \otimes p(t) + \upsilon_1(t) \tag{1}$$

$$r_2(t) = s_2(t) + \upsilon_2(t) = s\left(\frac{t}{a} - t_o\right) \otimes p(t) + \upsilon_2(t) \tag{2}$$

where, $r_1(t)$ and $r_2(t)$ represent, respectively, the pre- and postcompression rf echo signals, $s(t)$ represents the 1-D ultrasound scattering function, $p(t)$ represents the point-spread function (PSF), a represents the compression factor caused by axial-mechanical pressure to the medium, $\upsilon_1(t)$ and $\upsilon_2(t)$ are the uncorrelated random noise profiles and $\otimes$ represents the convolution operation. The strain $\in$ is related to the compression factor $1/a$ as,[28]

$$\in = 1 - a \tag{3}$$

where, $a \leq 1$ and $\in << 1$.

Strain estimation

Let $RF_1(i,j)$ and $RF_2(i,j)$ be the pre- and postcompression rf echo frames, respectively. i represents the axial depth index and j represents rf A-line index. Strain at a particular point on the strain map (i_s, j_s) is calculated from a corresponding pair of 1-D windowed pre- and postcompression rf segments, $r_1^{(r_s, j_s)}$ and $r_2^{(r_s, j_s)}$, respectively. These segments are selected as

$$r_1^{(i_S, j_S)}(i) = RF_1((i_s - 1)D_v + i, j), \qquad \text{for } 1 \leq i \leq L_i \text{ and } j = j_s \tag{4}$$

$$r_2^{(i_S, j_S)}(i) = RF_2(round((i_s - 1)(1 - s_{ap})D_v) + i, j), \tag{5}$$

for $1 \leq i \leq L_i$ and $j = j_s$ and $j = j_s + (j_s - \frac{N_a}{2}) s_{ap} \nu_v$

where, s_{ap} represents the approximate applied strain, N_a represents the total number of A-lines in the ultrasound images, D_v represents the distance between samples of the two rf

echo segments in the axial direction and L_i represents the length of the 1-D rf window. The axial mechanical stress causes a lateral shift of tissue segments. So, the value of j in $r_2^{(r_s, j_s)}$ deviates from actual j_s. Therefore, the Poisson's ratio is used to interpolate the postcompression data window for reducing the lateral shift effect in axial strain calculation. It is assumed that the center A-line (i.e., $round(N_a/2)$) experiences no lateral shift but the zero-lateral-shift line may differ slightly from a straight line and may not go through the middle exactly.

Before displacement estimation, global stretching on postcompression signal window is performed to reduce decorrelation noise. If the postcompression signal is stretched by a factor α, then Eq. (2) yields,[10]

$$r_\alpha(t) = r_2(\alpha t) = s_\alpha(t) + \upsilon_\alpha(t) = s\left(\frac{\alpha}{a}t - t_o\right) \otimes p(\alpha t) + \upsilon_2(\alpha t) \tag{6}$$

In a similar fashion, after stretching the postcompression echo window $r_2^{(r_s, j_s)}$ by a factor α (≤ 1), i.e., $r_\alpha^{(r_s, j_s)}(i) = r_2^{(r_s, j_s)}(\alpha i)$, the NCC coefficient $\rho_\alpha^{rf}(k)$ between $r_1^{(r_s, j_s)}$ and $r_\alpha^{(r_s, j_s)}$ is calculated as[29]

$$\rho_\alpha^{rf}(k) = \frac{\sum_{i=1}^{L_i} r_1^{(i_s, j_s)}(i).r_\alpha^{(i_s, j_s)}(i+k)}{\sqrt{\sum_{i=1}^{L_i}\{r_1^{(i_s, j_s)}(i)\}^2 \sum_{i=1}^{L_i}\{r_\alpha^{(i_s, j_s)}(i)\}^2}} \tag{7}$$

Eq. (7) becomes maximum for $\alpha = a$ with the approximation of $p(\alpha t) \approx p(t)$. This approximation is reasonably good up to moderate values of the applied strain. At high strain, this assumption may introduce bias in the strain estimates.

It is to be noted that the lesion area experiences much less or no compression depending on the stiffness of the mass. Therefore, to image the lesion boundary well, the global stretching effect is to be avoided in the lesion area. As the position of the lesion is typically unknown, we use an approach to calculate the NCC of the pre- and postcompression signal windows with and without global stretching. We use two different values of α (i.e., $\alpha_{max} = 1$ and $\alpha_{ap} = 1\text{-}s_{ap}$) for stretching the postcompression signal to compute the NCC function $\rho_\alpha(k)$.[30]

We compute the envelopes of the interrogative pre- and postcompression (stretched and nonstretched) data windows using the Hilbert transform (Eqs. (8) and (9)). Due to its asynchronous nature, the Hilbert transform does not need the center frequency of the ultrasound system to compute the envelope.

$$e_1^{(i_s, j_s)} = \left|Hilbert[r_1^{(i_s, j_s)}(i)]\right| \tag{8}$$

$$e_\alpha^{(i_s, j_s)} = \left|Hilbert[r_\alpha^{(i_s, j_s)}(i)]\right| \tag{9}$$

where *Hilbert* denotes the Hilbert transform. Like Eq. (7), the envelope NCC function is calculated as

$$\rho_\alpha^{env}(k) = \frac{\sum_{i=1}^{L_i} e_1^{(i_s, j_s)}(i).e_\alpha^{(i_s, j_s)}(i+k)}{\sqrt{\sum_{i=1}^{L_i}\{e_1^{(i_s, j_s)}(i)\}^2 \sum_{i=1}^{L_i}\{e_\alpha^{(i_s, j_s)}(i)\}^2}}$$

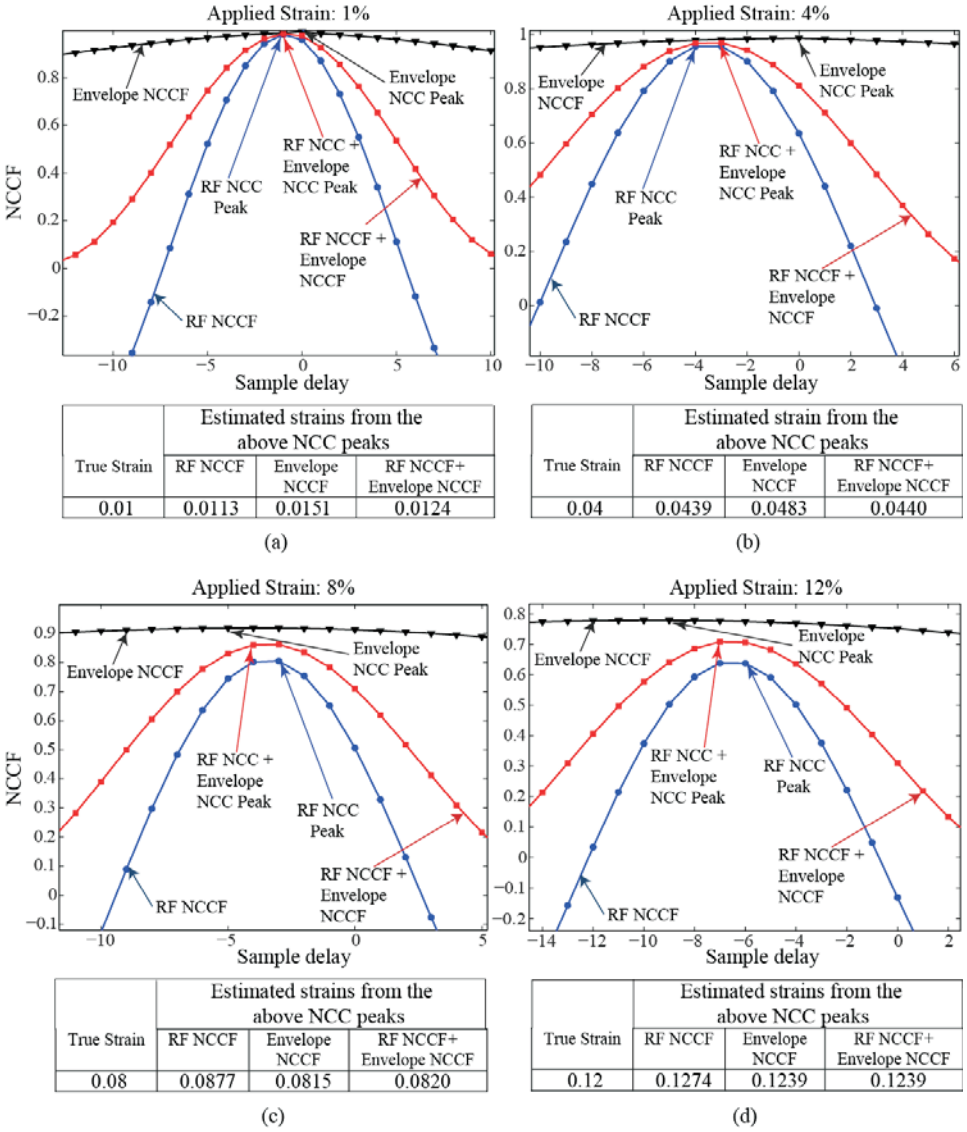

True Strain	Estimated strains from the above NCC peaks		
	RF NCCF	Envelope NCCF	RF NCCF+ Envelope NCCF
0.01	0.0113	0.0151	0.0124

(a)

True Strain	Estimated strain from the above NCC peaks		
	RF NCCF	Envelope NCCF	RF NCCF+ Envelope NCCF
0.04	0.0439	0.0483	0.0440

(b)

True Strain	Estimated strains from the above NCC peaks		
	RF NCCF	Envelope NCCF	RF NCCF+ Envelope NCCF
0.08	0.0877	0.0815	0.0820

(c)

True Strain	Estimated strains from the above NCC peaks		
	RF NCCF	Envelope NCCF	RF NCCF+ Envelope NCCF
0.12	0.1274	0.1239	0.1239

(d)

FIG. 1 Zoomed views of the normalized cross-correlation functions (NCC function) *vs.* sample delay for a particular point on the strain image of the FEM phantom at (a) 1%, (b) 4%, (c) 8% and (d) 12% strain. The point is chosen from the homogeneous background. The corresponding true and calculated strain values are also shown in tabular form at the bottom of the respective NCC function plot.

For robust strain estimation, we add weighted NCC functions and computed for the same interrogative data windows to generate a true peak. A piecewise linear weight, *LW*, is defined from our observation to control the contribution of the rf and envelope NCC functions in the combined NCC function. It is to be noted that the amount of echo decorrelation due to the increase of the applied strain may depend on the data types (e.g., computer-simulated phantom, tissue-mimicking phantom, *in-vivo* patient data, etc.). However, at a very low strain, rf NCC function alone works better than the sum. The effectiveness of using the weighted summation of the rf NCC function and envelope NCC function are illustrated in figure 1. A particular point on the strain map is chosen from the homogeneous background of the FEM-simulation phantom. The rf NCC function, envelope NCC function and the sum of

the equally-weighted rf and envelope NCC functions of that particular point are plotted for 1%, 4%, 8% and 12% applied strain in figures 1(a)-(d), respectively. The strain values calculated from these plotted peaks of the rf NCC function, envelope NCC function and the sum of the equally weighted rf and envelope NCC functions are shown at the bottom of each plot. We can see from figures 1(a)-(d) that with increase of applied strain, the rf NCC function estimate of the strain deteriorates. In contrast, the envelope NCC function generates strain closer to the true value with increase of the applied strain. Consequently, the sum of the weighted rf NCC function and envelope NCC function generates better strain values than that of the rf NCC function at high applied strain. We can also see from figures 1(c), (d) for 8% and 12% applied strains that the peaks of the rf NCC fall below 0.9, which is a clear depiction of the increased echo decorrelation.

Considering the above, *LW* is defined as (details are discussed in the result section)

$$LW = \begin{cases} 0 & for \quad s_{ap} \le s_{knee} \\ \dfrac{0.5(s_{ap} - s_{knee})}{s_{\max} - s_{knee}} & for \quad s_{knee} < s_{ap} \le s_{\max} \\ 0.5 & for \quad s_{ap} > s_{\max} \end{cases} \tag{10}$$

Here, s_{knee} denotes the 'knee strain,' $s_{\max}$ denotes the maximum strain and s_{ap} denotes the approximate applied strain.

Using *LW*, the robust NCC function is calculated as

$$\rho_{\alpha}(k) = LW \times \rho_{\alpha}^{env}(k) + (1 - LW) \times \rho_{\alpha}^{rf}(k) \tag{11}$$

From the NCC functions, the discrete time-lag is calculated as

$$k_{\alpha}^{(i_s, j_s)} = \arg\max_{k}\{\rho_{\alpha}(k)\}, \qquad \text{for } a = a_{max} \text{ and } \alpha_{ap}$$

We use a cosine interpolation algorithm to calculate the subsample time-lag values. Finally, the displacement is calculated as

$$D(i_s, j_s) = \begin{cases} k_{\alpha_{ap}}^{(i_s, j_s)} + k_{comp} + \dfrac{L_i}{2} s_{ap} & for \quad \beta \ge \gamma \\ k_{\alpha_{\max}}^{(i_s, j_s)} + k_{comp} & for \quad Otherwise \end{cases} \tag{12}$$

where $\beta = \rho_{\alpha_{ap}}^{(i_s, j_s)}(k_{\alpha_{ap}}^{(i_s, j_s)})$, $\gamma = \rho_{\alpha_{\max}}^{(i_s, j_s)}(k_{\alpha_{\max}}^{(i_s, j_s)})$ and $k_{comp} = round((i_s - 1)\, a_{max} D_v) - (i_s - 1)\, D_v$. k_{comp} is the displacement compensated in the shifting operation (1-s_{ap}) for the window selection in Eq. (5). The compensated displacement in the stretching operation of the post-compression signal before the cross-correlation operation is reinstated by $(\frac{L_i}{2} s_{ap})$ in Eq. (12). Finally, from the displacement map $D(i_s, j_s)$, the strain $S(i_s, j_s)$ is calculated using the least-square-error-based strain estimation method[17] with four-points per strain estimate.

Diffusion filtering

In this article, we also introduce diffusion filtering in elastography for strain-image denoising. Preserving the lesion edge while denoising is very important in the field of medical imaging. The diffusion filter performed well in this regard in the field of X-ray and CT imaging. Here, we use the geometric nonlinear diffusion filter.[27] The strain-image update equation is,

$$I_s^n = I_s^{n-1} + \Delta t[C(D_x, P_x).(\nabla_E + \nabla_W) + C(D_y, P_y).(\nabla_N + \nabla_S)]^{n-1}$$

Here, I_s^0 is the original strain image and I_s^n ($n > 0$) is the diffused strain image at the nth step, $\nabla_p = I_p - I_s$ ($p = E, W, N$ and S) denotes the difference between the interrogative pixel and one of the east, west, north and south pixels, respectively, n is the iteration number, Δt is the integration constant and C is the sigmoid diffusivity function defined as

$$C(D_a, P_a) = \frac{1}{1 + \exp\{(-|P_a| - |D_a|) \times 50\}}$$

where a represents x or y directions, D_a denotes the a-directional intensity difference in a 3×3 window and P_a is defined from D_a depending on a threshold value of the image intensity of the interrogative pixel.[27] We use $1 \le n \le 10$ and $\Delta t = 0.15$.

SIMULATION AND EXPERIMENTAL RESULTS

In this section, we first define the piecewise linear weight to be used in strain calculation for different types of data. In subsequent subsections, we show the efficacy of using the Poisson's ratio and provide comparative results of our proposed method with the novel spline-based approach for robust strain estimation in elastography (SBSE)[9] and ultrasound elastography performance enhancement with the wavelet denoising (UPWD)[19] method using the (FEM) phantom, CIRS (CIRS, Inc., Norfolk, VA) experimental phantom and the *in vivo* patient data. In addition to subjective evaluation by visual inspection, we compare the performances of different methods in terms of several numerical indices: elastographic signal-to-noise ratio (SNRe),[31] elastographic contrast-to-noise ratio (CNRe)[32] and mean structural similarity (MSSIM).[33]

Piecewise linear weight

We observed in our investigation that giving equal weight to both the rf NCC function and envelope NCC function works the best at high strain. The maximum value of the strain (defined as $s_{\max}$ in Eq. (10)) may be assumed to be equal or greater than 0.1, 0.05 and 0.03 for the FEM simulation, experimental phantom and *in vivo* breast data, respectively, as greater than these values might be unrealistic for each of the cases. However, at a low strain, the rf NCCF alone works better than the sum. Therefore, we define some 'knee' strain points for the FEM phantom, experimental phantom and *in vivo* data in terms of the NCC peaks; the envelope NCC function is to be added with the rf NCC function for better strain estimation only when the applied strain is greater than this knee value. For defining the knee for a particular data type, NCC peaks are calculated for a background region of the respective strain map. We know that, with the increase of applied strain, echo decorrelation increases by different rates

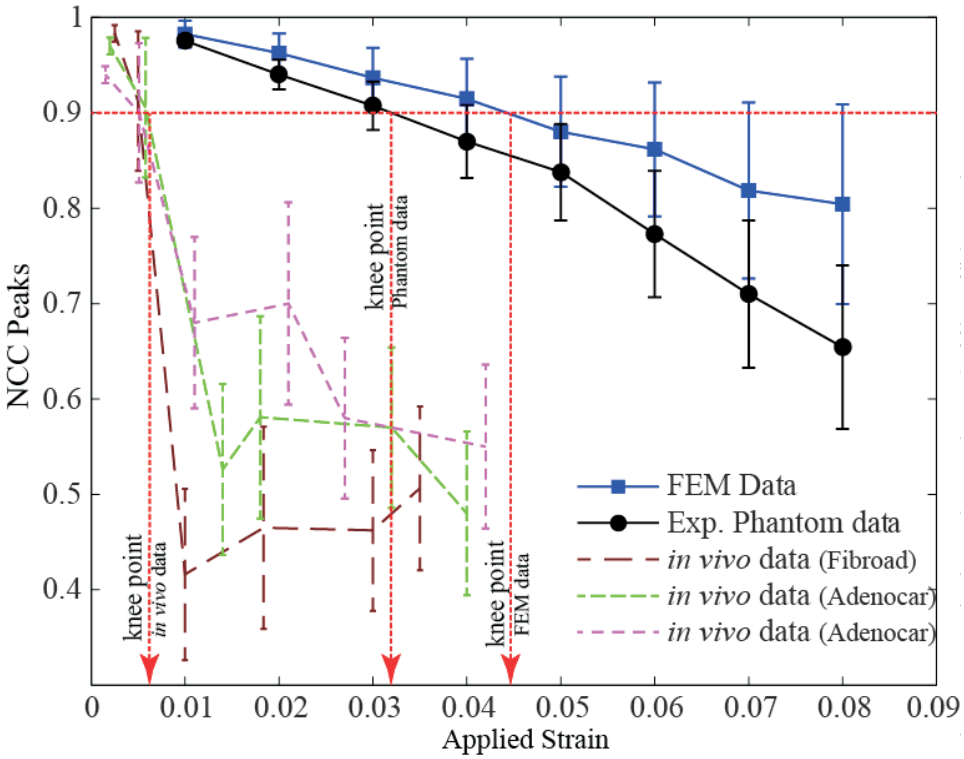

FIG. 2 Representation of the normalized cross-correlation (NCC) peaks *vs.* applied strain for the FEM phantom, experimental phantom and *in vivo* data. By taking the NCC peak value 0.9 as a threshold, some knee strain points are defined for the FEM phantom, experimental phantom and *in vivo* data.

depending on the data types and, consequently, the NCC peaks falls off rapidly. We choose 0.9 as the NCC peak threshold and the knee point is defined as that particular value of the applied strain, greater than which the NCC peak falls below this threshold (see figure 2). However, the envelope NCC peak may be greater than 0.9 for a large range of the applied strain, even for the strain greater than the knee point for all three types of data. But the peak position is not precise enough at a low strain, thereby leading to a very noisy strain image. To define a knee point for the *in vivo* data in figure 2, we use three patient cases where one is fibroadenoma and two are adenocarcinoma cases. In figure 3, the piecewise linear weight is graphically presented and from this figure, knee strain can be assumed to be 0.045, 0.03 and 0.005 for the FEM phantom, experimental phantom and *in vivo* data, respectively.

FEM simulation

A rectangular phantom of 40 mm × 40 mm was simulated using the Algor (FEM) software (Algor, Inc., Pittsburgh, PA). It has a homogeneous background with the stiffness of 60 kPa. A 60 kPa stiffness is close to the average stiffness of normal glandular tissue in the breast.[34] The phantom has four circular inclusions of 7.5mm diameter each (Fig. 4(a)). The bottom left, top, bottom right and middle inclusions were 10, 20, 30 and 40 dB (or 3.16, 10.00, 31.62 and 100.00 times) stiffer than the background, respectively. The bottom of the phantom was placed on a planar surface and the phantom was in full-slip condition. During the simulation, the Poisson's ration was used as 0.495. The phantom was scanned from the top with a probe of center frequency, f_0 = 5 MHz and 60% bandwidth. A nondiffracting transducer beam was

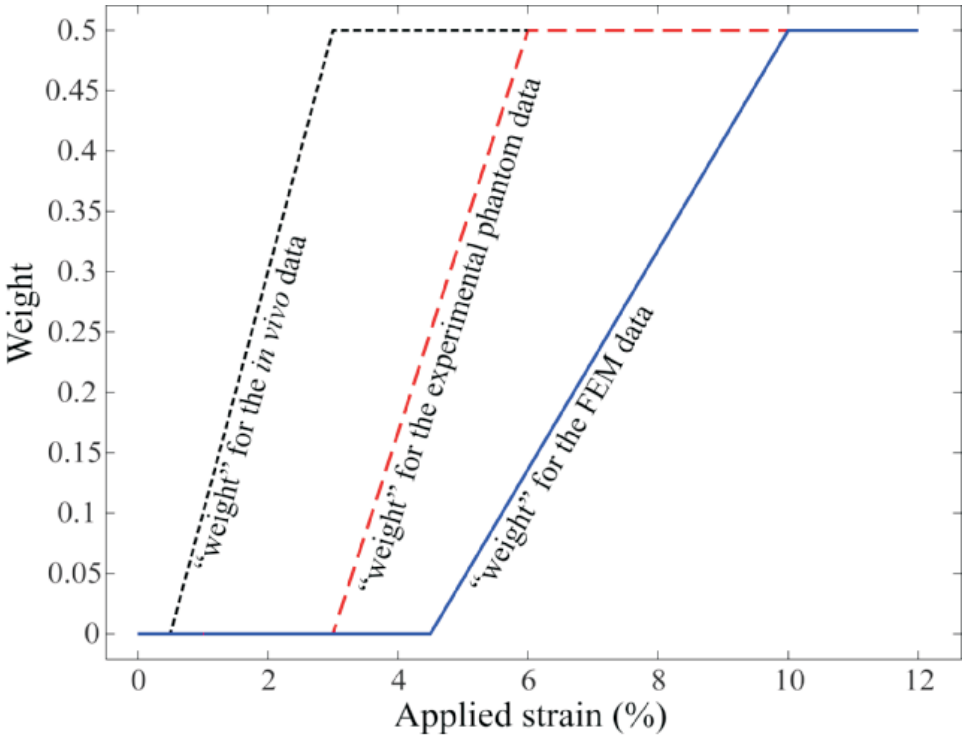

FIG. 3 Graphical presentation of the piecewise linear weight (*LW*) for different data types at different percentages of the applied strain

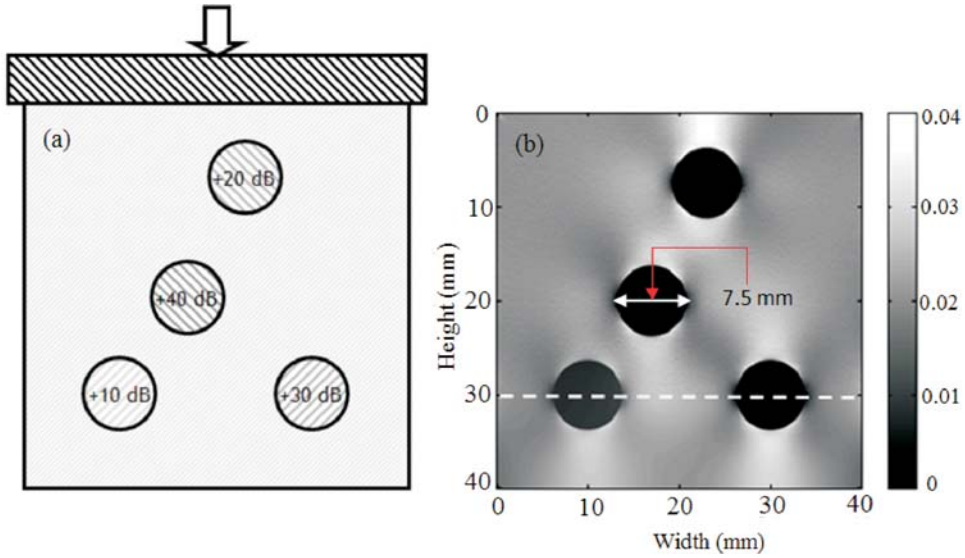

FIG. 4 (a) FEM simulation phantom. It contains four stiff inclusions in a homogeneous background of 60kPa. (b) Corresponding ideal elastogram.

simulated with a beam width of 1.5 mm. The total number of A-lines was 128. White noise of a random nature was added to simulate a sonographic SNR of 40 dB.[9] Figure 4(b) represents the ideal elastogram for a 2% applied strain.

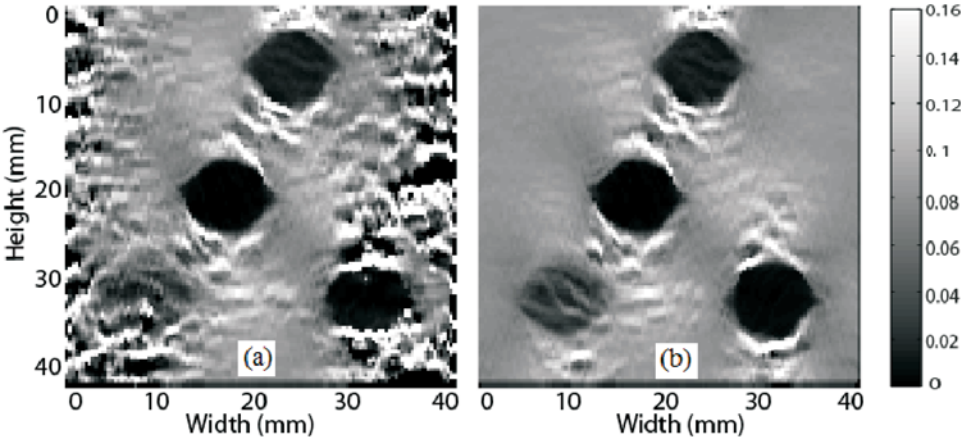

FIG. 5 Effects of using Poisson's ratio at 8% strain. Strain images generated (a) without using Poisson's ratio and (b) using Poisson's ratio.

To show the effect of using the Poisson's ratio for strain estimation, two strain images at 8% applied strain are shown in figure 5. It is clear from figure 5(a) that it is very noisy in both the left and right sides resulting in lesion edges at bottom that are not clearly visible. On the other hand, figure 5(b) does not suffer from the same noise.

In figures 6(a)-(t), we show the strain images generated by the SBSE, Eq. (12) with rf NCC (RFC), Eq. (12) with weighted rf and envelope NCC (W-RFENV), proposed DIFF method (W-RFENV with diffusion filtering) and UPWD with W-RFENV as the basic method for four different applied strains. In all the methods, we have used a data window (L_i) size of 2.28mm and an interwindow shift (D_y) of 0.28mm. From these figures, it is easily observable for 2% strain that the SBSE produces somewhat noisy strain image in contrast to the images formed by the proposed method. The distortion is severe in figures 6(b)-(d) for 6%-10% strains, respectively, and the inclusions disappear. The strain image for the RFC method is degraded by noise at 8% and 10% strains. On the contrary, the W-RFENV method generates very clean strain image at all strains from 2% to 8% while a little noisy at 10%, indicating the superiority of this method. The diffusion-filtered strain images produced by the W-RFENV method (DIFF) are the best for each of the strain cases and the background has become almost smooth with each of the lesion edges preserved. The wavelet-based UPWD method smoothes all the images without lesion edges preserved.

Three numerical indices, SNRe, CNRe and MSSIM, are graphically presented in figure 7 to evaluate the strain-image quality generated by the SBSE, RFC, W-RFENV, DIFF and UPWD with the basic method W-RFENV. In the SNRe plot, the W-RFENV shows better performance than the RFC at high strains and the DIFF can be said to be the best among all the methods. Although the UPWD shows better performance, it does not preserve the lesion edges at all (Figs. 6(s)-(t)). In the CNRe plot, the W-RFENV shows better performance than the RFC at higher strains and the DIFF shows the expected best performance but the UPWD makes the performance worse than its basic method while the SBSE is at the bottom. In the MSSIM plot, although the DIFF and UPWD are close, the latter has bad impact on the lesion edges, as evident from figure 6. Therefore, the DIFF can be said to be the best.

Phantom experiment

We use a tissue-mimicking (TM) phantom (CIRS, Inc. Norfolk, VA) of dimension 90 mm × 90 mm × 120 mm with a 3× stiffer (compared to the surrounding) cylindrical inclusion of 2

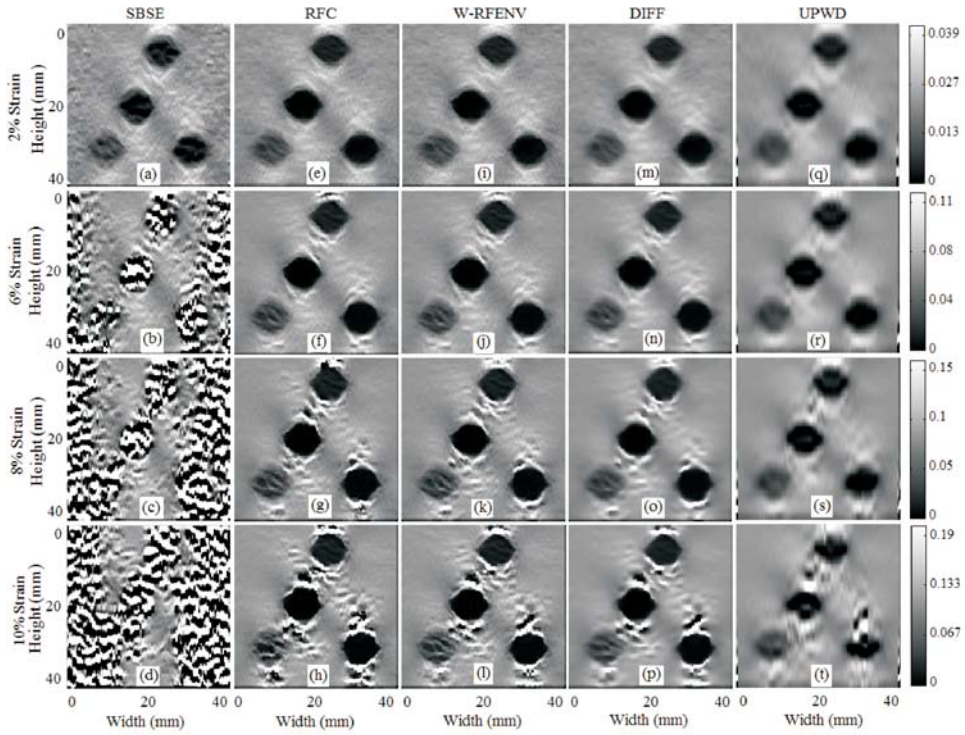

FIG. 6 Strain images of the FEM simulation phantom generated by different methods. Results (a)-(d) are produced by the SBSE,[9] (e)-(h) are produced by the RFC ($\nu_v = 0.5$), (i)-(l) are produced by the W-RFENV ($\nu_v = 0.5$), (m)-(p) are the diffusion-filtered images of (i)-(l) and (q)-(t) are produced by the UPWD.[19]

cm diameter to perform the elastography experiment. In the experiment, an ATL (Bothell, WA) Ultramark 9 scanner with a 7.5MHz linear array transducer was used to acquire rf-echo signals from this CIRS phantom. The rf-echo sampling frequency was 20 MHz and quantized at 14 bits/sample. Before processing the rf data, it was corrected for time-gain-control (TGC).

Figures 8(a)- (j) exhibit the strain images generated by the SBSE, RFC, W-RFENV, DIFF and UPWD with the basic method W-RFENV for two different strains, respectively. The strain image generated by the DIFF method (Fig. 8(g)) performs the best amongst all the methods for 3% strain while other methods are fairly good except that the UPWD method smoothes the strain image (Fig. 8(i)) at such a level that the lesion visibility is significantly reduced. At 5% strain, the SBSE method produces a very noisy strain map but the strain map generated by the RFC method is less noisy in the background. The lesion area of the strain image generated by the W-RFENV method is less noisy than that of the RFC method for 5% strain. The DIFF method produces a much smoother strain map and, therefore, the lesion and the background are distinguishable in the presence of noise at 5% applied strain. The UPWD method smoothes the strain map without preserving the lesion edges (Fig. 8(j)).

To evaluate the strain image quality of the CIRS phantom at two different applied strains, the SNRe and CNRe are presented in a table for the SBSE, RFC, W-RFENV, DIFF and UPWD with the basic method W-RFENV (Fig. 9(b)). Regarding SNRe, it is seen from the table that the DIFF shows the best performance among all the methods for 3% strain. At 5% strain, the W-RFENV shows better performance than the RFC, SBSE and UPWD methods, as expected, while the DIFF-generated strain image exhibits the highest SNRe value. Regarding CNRe, we see from the table that the RFC shows better performance than the SBSE and UPWD methods and DIFF shows the best performance for 3% strain. At 5% strain,

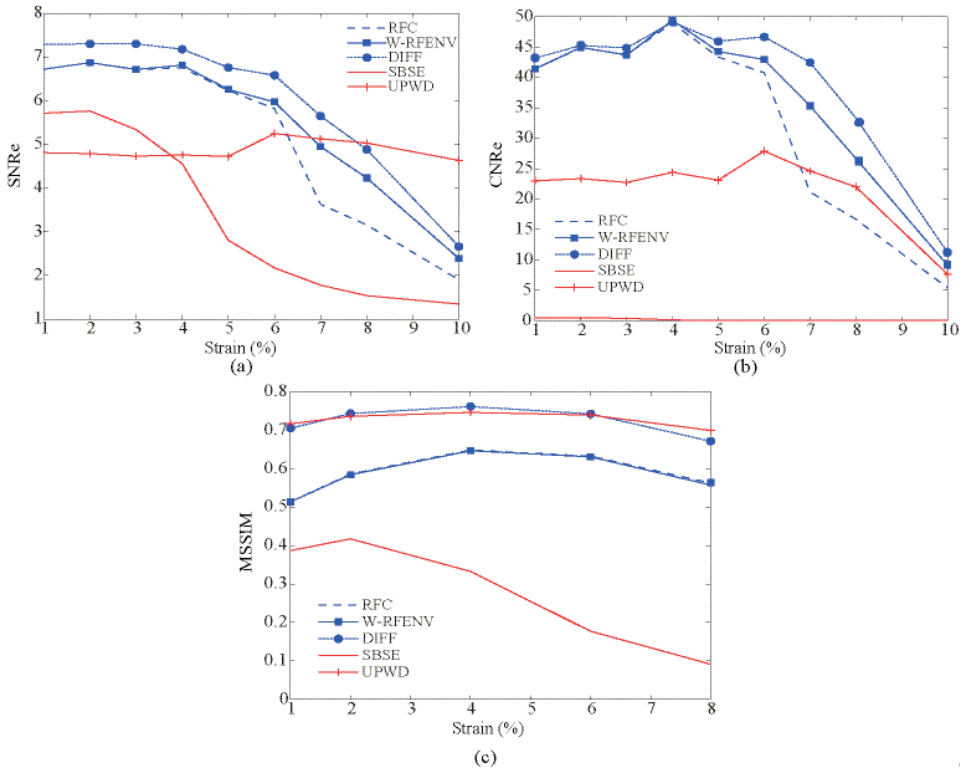

FIG. 7 Performance comparisons of different methods using numerical indices. (a) SNRe *vs.* applied strain (b) CNRe *vs.* applied strain and (c) MSSIM *vs.* applied strain.

W-RFENV shows better performance, as expected, than the RFC, SBSE and UPWD methods and the CNRe value of the DIFF-generated strain image is found to be the maximum.

In vivo breast experiment

We chose *in vivo* breast data for this work from an existing database of 33 cases (patients' age: 20-75 years). These data were acquired with free-hand compression; benign and malignant cases were confirmed by histopathological reports. A Sonix-500RP (Ultrasonix Medical Corporation, Richmond BC, Canada) scanner operating at 10 MHz (nominal) was used to acquire these data at the University of Vermont, USA. The institutional review board (IRB) approved this study and consent was obtained from patients. Out of 33 cases, two cases are selected in this work, one of which is a high strain frame (applied strain is approximately 2.5%, patient is 63 years old and has an adenocarcinoma) and another one is a low strain frame (applied strain is approximately 0.7%, patient is 38 years old and has a fibroadenoma).

In figures 10(b)-(f), strain images are produced by the SBSE, RFC, W-RFENV, DIFF and UPWD with the basic method W-RFENV, respectively, for patient-I and, in figures 10(h)-(l), strain images are produced by the SBSE, RFC, W-RFENV, DIFF and UPWD with the basic method W-RFENV, respectively, for patient-II. We have also calculated the MSSIM of each of the images by choosing two strain images (Figs. 11(a) and 11(c) generated by Hasan et al[26] as references for patient-I and patient-II, respectively. For patient-I, we can see from 10(b)-(f) that except for the SBSE and UPWD, all other methods show good performance in extracting the cancerous lesion from the backscattered ultrasound rf signals.

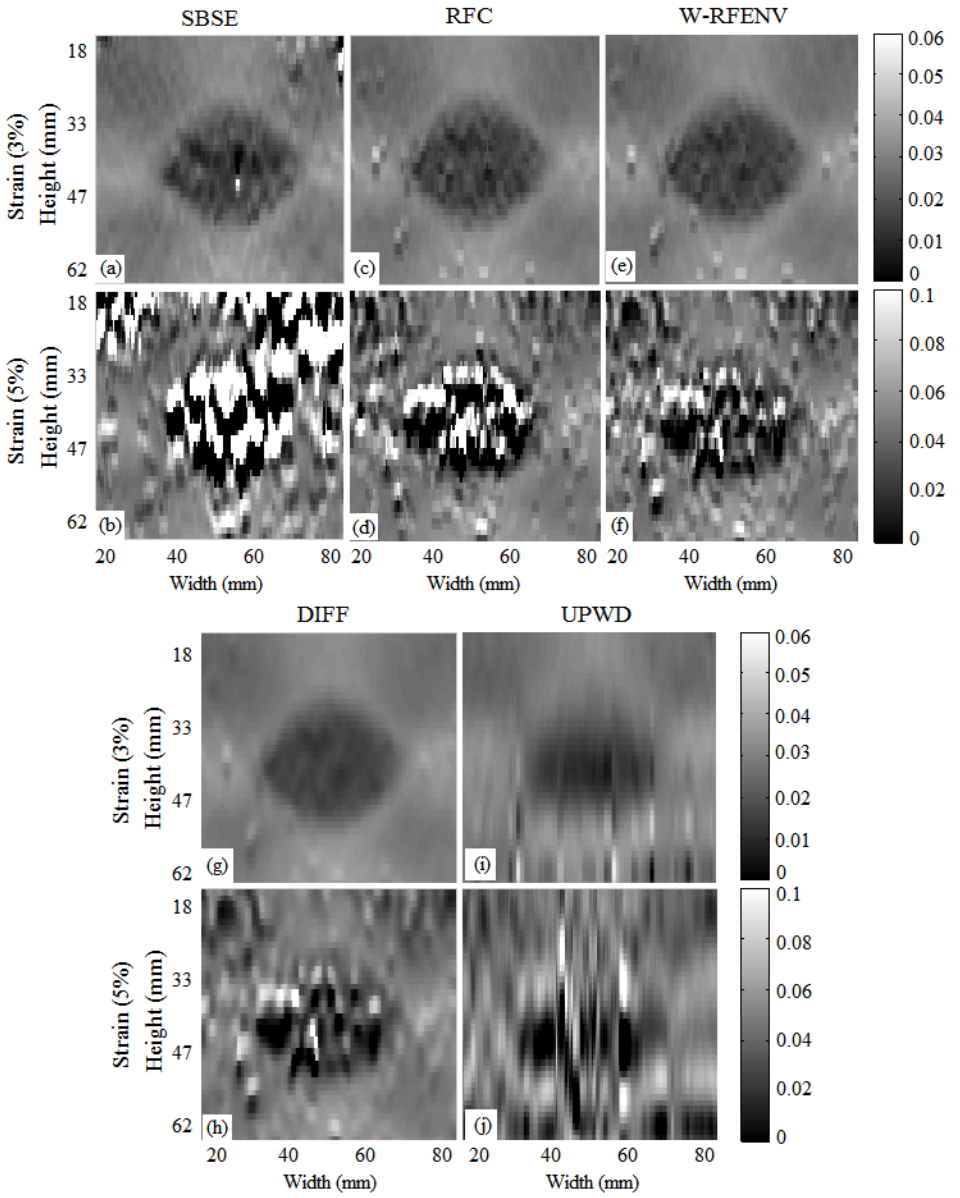

FIG. 8 Strain images of the CIRS experimental phantom generated by different methods. Results (a)-(b) are produced by the SBSE, (c)-(d) are produced by the RFC (ν_v= 0.5), (e)-(f) are produced by the W-RFENV (ν_v = 0.5), (g)-(h) are the diffusion-filtered images of (e)-(f) (DIFF) and (i)-(j) are produced by the UPWD.

For patient-II, only the SBSE method performs poorly among all other methods (Fig. 10(h)). The DIFF method shows a smoother background compared to other approaches. In figures 10(c)-(d), strain images generated by the RFC and W-RFENV techniques appear similar in open eyes. But from the MSSIM table in figures 11(b) and (d), it is seen that the W-RFENV shows better performance than the RFC. The DIFF shows the best performance in terms of MSSIM (Figs. 11(b) and 11(d)). However, the UPWD shows very poor performance in generating the strain images (Figs. 10(f) and 11(b)) for patient-I and (Figs. 10(l) and 11(d)) for patient-II.

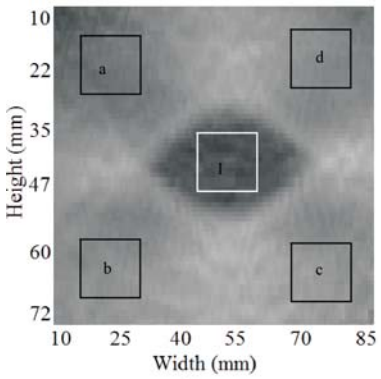

(a)

Methods	SNRe		CNRe	
	Strain (3%)	Strain (5%)	Strain (3%)	Strain (5%)
SBSE	11.7263	2.3572	12.7334	0.0153
RFC	11.0563	3.3183	39.5125	0.0918
W-RFENV	11.4713	4.5315	55.1831	1.8351
DIFF	13.0081	5.8701	75.8201	2.8563
UPWD	7.2315	2.3180	24.7815	0.7013

(b)

FIG. 9 (a) Strain image of the CIRS experimental phantom showing the lesion window-I and four background windows-a, b, c, d for the SNRe and CNRe calculation. (b) Table showing the SNRe and CNRe values for different methods at two different strains.

CONCLUSION

In this paper, we have proposed a noise-robust displacement and strain-estimation algorithm in the time domain. We have shown that the combined rf and envelope NCC can produce better strain images than the rf or the envelope NCC alone. We have also introduced diffusion filtering to denoise the strain map. Compared to other denoising filters, diffusion filter has the ability to preserve edges and, therefore, lesion edges can be preserved while denoising. The effect of considering the lateral shift in the selection of 1-D rf pre- and postcompression segments has also been shown in our method. Unlike conventional gradient-based strain estimators, our proposed method can image hard inclusions accurately. It has been shown by the simulation phantom, experimental phantom as well as by the *in-vivo* breast data that the proposed method is more robust for a wide range of strain values than the other techniques used for comparison in this paper. The quantitative performance indices also indicate that the proposed method can generate high-quality strain images at high strain than that of the techniques compared in the literature.

ACKNOWLEDGMENTS

This work has been supported by HEQEP UGC (CP#96/BUET/Win-2/ST(EEE)/2010), Bangladesh, in part by Susan G. Komen for the Cure grant KG081601, and National Research Foundation of Korea grant funded by the Korean government (2009-0078310). The elastography phantom used in this study was manufactured by CIRS, Inc. (Norfolk, VA). The phantom data were acquired by Sarayu Ramachandran, Andy Kalisz and Shreedevi Dasgupta, Riverside Research, New York, NY. *In vivo* breast data were acquired by Louise M. Mobbs and Dr. Brian S. Garra, Department of Radiology, Fletcher Allen Health Care, Burlington, VT.

REFERENCES

1. Garra B, Cespedes I, Ophir J, et al. Elastography of breast lesions: initial clinical results, *Radiology 202*, 79–86 (1997).

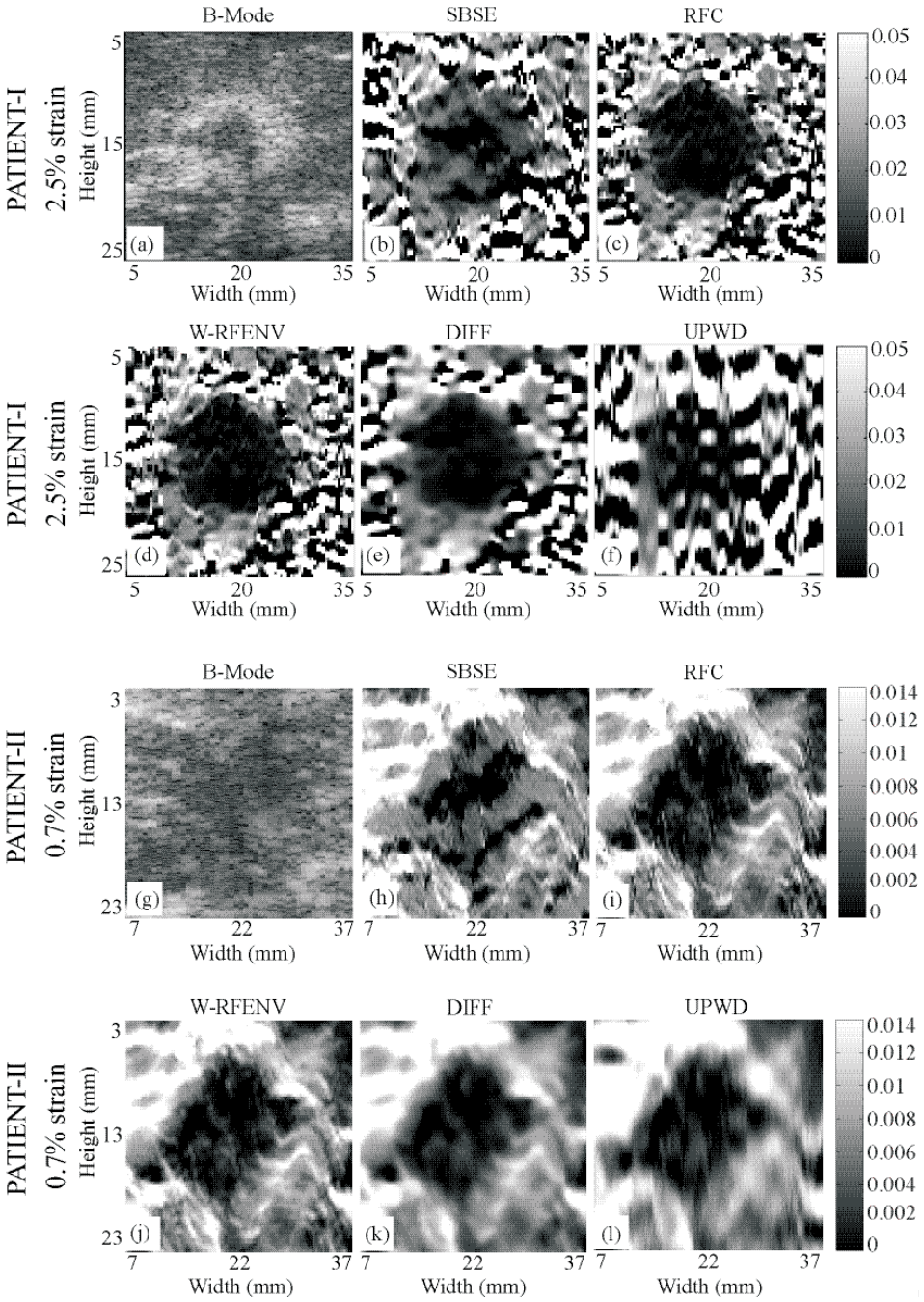

FIG. 10 Strain images generated by different methods using *in vivo* breast ultrasound data. (a) and (g) represent B-mode images of two patients. Results (b) and (h) are produced by the SBSE method, (c) and (i) are produced by the RFC method ($\nu_v = 0.5$), (d) and (j) are produced by the W-RFENV method ($\nu_v = 0.5$), (e) and (k) are the diffusion-filtered (DIFF) images of (d) and (j), respectively, and, (f) and (l) are produced by the UPWD method.

2. Ophir J, Cespedes I, Ponnekanti H, et al. Elastography, a quantitative method for imaging the elasticity of biological tissue, *Ultrasonic Imaging 13*, 111-134 (1991).

3. Ophir J, Cespedesa I, Garra BS, et al. Elastography: ultrasonic imaging of tissue strain and elastic modulus in vivo, *Eur J Ultrasound 3*, 49-70 (1996).

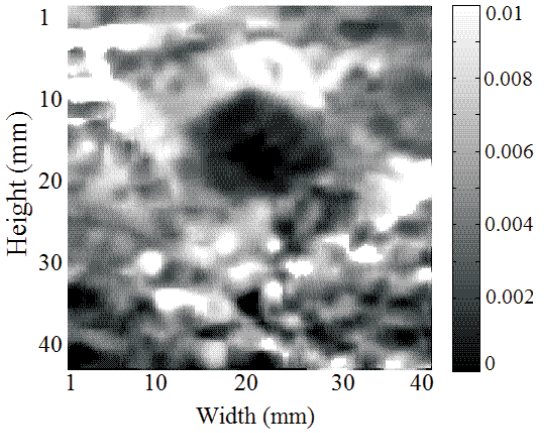

(a)

Methods	MSSIM (%)
SBSE	1.63
RFC	1.75
W-RFENV	1.81
DIFF	2.83
UPWD	0.47

Patient Specification: 63/Adenocar

(b)

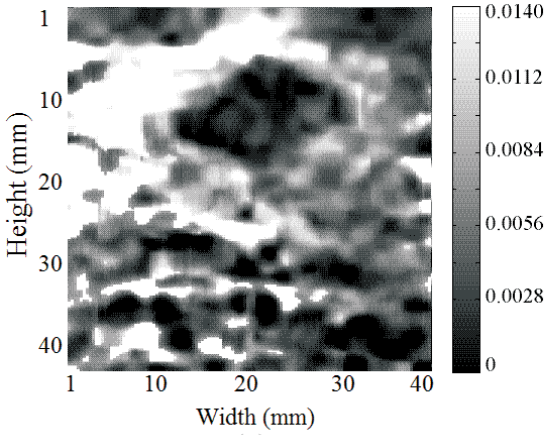

(c)

Methods	MSSIM (%)
SBSE	11.02
RFC	19.16
W-RFENV	21.52
DIFF	29.99
UPWD	26.94

Patient Specification: 38/Fibroad

(d)

FIG. 11 (a) Reference strain image of the *in vivo* breast data generated by Hasan et al[26] for patient-I at approximately 0.5% applied strain, (b) Table showing the MSSIM values of different methods for patient-I. (c) Reference strain image generated by Hasan et al[26] for patient-II at approximately 0.5% applied strain, (d) Table showing the MSSIM values of different methods for patient-II. Here, the reference images are produced at low strain (0.5%) to get better image quality.

4. Cespedes I, Ophir J, Ponnekanti H, et al. Elastography: Elasticity imaging using ultrasound with application to muscle and breast *in vivo, Ultrasonic Imaging 15*, 73-88 (1993).

5. Friedrich-Rust M, Ong MF, Herrmann E, et al. Real-time elastography for noninvasive assessment of liver fibrosis in chronic viral hepatitis, *Amer J Roentgen 188,* 758-764 (2006).

6. Korte CL, Van der Steen AFW. Intravascular ultrasound elastography: an overview, *Ultrasonics 40,* 859-865 (2002).

7. Ophir J, Alam SK, Garra BS, et al. Elastography: imaging the elastic properties of soft tissues with ultrasound, *J Med Ultrasound 29*, 155–171 (2002).

8. Azar RZ, Salcudean SE. Motion estimation in ultrasound images using time domain cross correlation with prior estimates, *IEEE Trans Biomed Eng 53*, 1990-2000 (2006).

9. Alam SK. Novel spline-based approach for robust strain estimation in elastography, *Ultrasonic Imaging 32,* 91-102 (2010).

10. O'Donnell M, Skovoroda AR, Shapo BM, et al. Internal displacement and strain imaging using ultrasonic speckle tracking, *IEEE Trans Ultrason Ferroelectr Freq Contr 41,* 314-325 (1994).

11. Alam SK, Ophir J, Konofagou EE, An adaptive strain estimator for elastography, *IEEE Trans Ultrason Ferroelectr Freq Contr 45,* 461-472 (1998).

12. Varghese T, Konofagou EE, Ophir J, et al. Direct strain estimation in elastography using spectral cross-correlation, *Ultrasound Med Biol 26,* 1525-1537 (2000).

13. Alam SK, Lizzi FL, Varghese T, et al. Adaptive spectral strain estimators for elastography, *Ultrasonic Imaging 26,* 131-149 (2004).

14. Srinivasan S, Krouskop T, Ophir J. Comparing elastographic strain images with modulus images obtained using nanoindentation: preliminary results using phantoms and tissue samples, *Ultrasound Med Biol 30*, 329-343 (2004).

15. Varghese T, Ophir J. Performance optimization in elastography: multicompression with temporal stretching, *Ultrasonic Imaging 18,* 193-214 (1996).

16. Konofagou EE, Ophir J, Kallel, et al. Elastographic dynamic range expansion using variable applied strains, *Ultrasonic Imaging 19,* 148–166 (1997).

17. Kallel F, Ophir J. A least-squares strain estimator for elastography, *Ultrasonic Imaging 19,* 185-208 (1997).

18. Techavipoo U, Varghese T. Wavelet denoising of displacement estimates in elastography. *Ultrasound Med Biol 30,* 477–491 (2004).

19. Cui S, Peng C, Chen X, et al. Ultrasound elastography performance enhancement using wavelet denoising, *Int. Conf Audio Lang Image Proc (ICALIP)*, pp. 1238-1243 (2010).

20. Alam SK, Ophir J. Reduction of signal decorrelation from mechanical compression of tissues by temporal stretching-applications to elastography, *Ultrasound Med Biol 23,* 95-105 (1997).

21. Chen H, Shi H, Varghese T. Improvement of elastographic displacement estimation using a two-step cross-correlation method, *Ultrasound Med Biol 33,* 48-56 (2007).

22. Varghese T, Ophir J. Characterization of elastographic noise using the envelope of echo signals, *Ultrasound Med Biol 24,* 543-555 (1998).

23. Chen L, Housden RJ, Treece GM, et al. A hybrid displacement estimation method for ultrasonic elasticity imaging, *IEEE Trans Ultrason Ferroelectr Freq Contr 57,* 866-882 (2010).

24. Shi H, Varghese T. Two-dimensional multi-level strain estimation for discontinuous tissue, *Phys Med Biol 52,* 389-401 (2007).

25. Shiina T, Doyley MM, Bamber JC. Strain imaging using combined RF and envelope autocorrelation processing, in *Proc IEEE Ultrasonics Symp*, pp. 13311336 (1996).

26. Hasan MK, Anas EMA, Alam SK, et al. Direct mean strain estimation for elastography using nearest-neighbor weighted least-squares approach in the frequency domain, *Ultrasound Med Biol* (May, 2012, in press).

27. Gonzalez EM, Cho MH, Lee SH. Geometric nonlinear diffusion filter and its application to X-ray imaging, *BioMed Engin Online 10:47* (2011).

28. Bilgen M, Insana MF. Deformation models and correlation analysis in elastography, *J Acoust Soc Amer 99,* 3212-3224 (1996).

29. Pan B, Qian K, Xie H, et al. Two-dimensional digital image correlation for in-plane displacement and strain measurement: a review, *Measurement Sci Tech 20*, 1-17 (2009).

30. Alam SK. A novel and robust method for rapid strain estimation in elastography, *Ultrasonic Imaging 26,* 29-40 (2004).

31. Cespedes I, Ophir J. Reduction of image noise in elastography, *Ultrasonic Imaging 15*, 89-102 (1993).

32. Varghese T, Ophir J. An analysis of elastographic contrast-to-noise ratio performance, *Ultrasound Med Biol 24,* 915-924 (1998).

33. Wang Z, Bovik HRS, Simoncelli EP. Image quality assessment: From error visibility to structural similarity, *IEEE Trans Image Process 134*, 600-612 (2004).

34. Krouskop TA, Wheeler TM, Kallel F, et al. Elastic moduli of breast and prostate tissues under compression, *Ultrasonic Imaging. 20*, 260-274 (1998).